Durham Research Online

Improved mass constraints for two nearby strong-lensing elliptical galaxies from *Hubble Space Telescope* imaging

William P. Collier,[★] Russell J. Smith and John R. Lucey

Centre for Extragalactic Astronomy, Departments of Physics, University of Durham, Durham DH1 3LE, UK

ABSTRACT

We analyse newly obtained *Hubble Space Telescope* imaging for two nearby strong lensing elliptical galaxies, SNL-1 ($z = 0.03$) and SNL-2 ($z = 0.05$), in order to improve the lensing mass constraints. The imaging reveals previously unseen structure in both the lens galaxies and lensed images. For SNL-1, which has a well resolved source, we break the mass-versus-shear degeneracy using the relative magnification information, and measure a lensing mass of $9.49 \pm 0.15 \times 10^{10}\,\mathrm{M_\odot}$, a 7 per cent increase on the previous estimate. For SNL-2, the imaging reveals a bright unresolved component to the source and this presents additional complexity due to possible active galactic nucleus microlensing or variability. We tentatively use the relative magnification information to constrain the contribution from SNL-2's nearby companion galaxy, measuring a lensing mass of $12.59 \pm 0.30 \times 10^{10}\,\mathrm{M_\odot}$, a 9 per cent increase in mass. Our improved lens modelling reduces the mass uncertainty from 5 and 10 per cent to 2 and 3 per cent, respectively. Our results support the conclusions of the previous analysis, with newly measured mass excess parameters of 1.17 ± 0.09 and 0.96 ± 0.10 for SNL-1 and SNL-2, relative to a Milky Way like (Kroupa) initial mass function.

Key words: gravitational lensing: strong – Galaxy: stellar content – galaxies: elliptical and lenticular, cD.

1 INTRODUCTION

Although rare in the Universe, galaxy-scale strong gravitational lenses provide the most precise and accurate total mass measurements (Treu 2010; Courteau et al. 2014). Unlike alternative mass estimators (such as stellar dynamics or spectroscopic analysis), strong lensing is unaffected by degeneracies due to the stellar population (e.g. age/metallicity), or structural properties (e.g. orbital anisotropy).

Gravitational lensing is sensitive only to the total [stars plus dark matter (DM)] mass projected within the Einstein radius (R_{Ein}). The stellar component within early-type galaxies (ETGs) is generally more centrally concentrated than the DM halo, which follows an extended profile (e.g. Navarro, Frenk & White 1996). Therefore, the fraction of mass contributed by the stars increases at smaller radius. Hence, for lenses in which the Einstein radius is small when compared to the galaxy's effective radius (R_{eff}), lensing provides a robust measurement of the *stellar* mass, which in turn provides information on the stellar initial mass function (IMF). In general, this scenario is best realized with low redshift lenses, where the critical density for lensing is higher, and exceeded only at small physical radius.

The three lowest redshift ($z \lesssim 0.05$) massive ETG lenses are ESO 325−G004, ESO 286−G022 and 2MASX J01414232−0735281. Whereas ESO 325−G004 was serendipitously discovered via *Hubble Space Telescope* (*HST*) imaging (Smith et al. 2005; Smith & Lucey 2013), the other two lenses were identified via targeted integral-field infrared spectroscopy with the SINFONI Nearby Elliptical Lens Locator Survey (SNELLS, Smith, Lucey & Conroy 2015, hereafter SLC15); we refer to these three galaxy lens systems as SNL-0, SNL-1 and SNL-2, respectively. The SLC15 lensing analysis of the SNELLS systems favoured a Milky Way (MW) like (Kroupa) IMF (Kroupa 2001) and is strongly inconsistent with the 'heavy' IMFs found in studies of massive ETGs via distant lenses, stellar dynamics and direct spectral analysis (Treu et al. 2010; Cappellari et al. 2012; Conroy & van Dokkum 2012).

The very local nature of the SNELLS sample allows the application of multiple independent IMF-determining techniques. High signal-to-noise ratio (S/N) optical spectra of the SNELLS lenses display features typical for a population of ETGs selected from SDSS to have similar velocity dispersions ($\sigma = 280\,\mathrm{km\,s^{-1}}$) (Newman et al. 2017, fig. 5). The spectral features for SNL-2 are found to be consistent with a MW-like IMF, in agreement with the lensing analysis, whereas SNL-1's spectra are found to favour a 'heavy' IMF. Furthermore, the stellar population synthesis modelling for SNL-1 finds a mass in excess of the total lensing mass

★ E-mail: william.p.collier@durham.ac.uk

Table 1. Galaxy properties of SNL-1 and SNL-2. The magnitudes are quoted in the observed frame. The quoted luminosities are corrected for band-shifting, derived from EZGAL (Mancone & Gonzalez 2012), and galactic extinction, from Schlafly & Finkbeiner (2011).

Quantity	SNL-1	SNL-2	Notes
NED ID	ESO 286−G022	2MASXJ01414232−0735281	
Lens z	0.0312	0.0519	
σ_{6dF} (km s^{-1})	356 ± 18	320 ± 18	Campbell et al. (2014)
$\sigma_{e/2}$ (km s^{-1})	289 ± 14	263 ± 13	Newman et al. (2017)
Source z	0.926	1.969	
Fiducial aperture, R_{ap} (arcsec)	2.38	2.21	SLC15, SINFONI based
$J(\leq R_{ap})$	12.80	13.53	PSF-corrected 2MASS
$I_{F814W}(\leq R_{ap})$	13.85 ± 0.02	14.53 ± 0.02	
$L_{F814W}(\leq R_{ap})$ (10^{10} L$_\odot$)	2.52 ± 0.04	3.86 ± 0.07	Extinction and band-shifting corrected
Half image-separation (arcsec)	2.43 ± 0.03	2.30 ± 0.03	This paper, *HST* based
$I_{F814W}(\leq$ separation)	13.83 ± 0.02	14.50 ± 0.02	
Flux ratio (A/B)	2.2 ± 0.1	2.5 ± 0.1	

estimated by SLC15. This result is further evidence of a tension between the results of different IMF estimators, motivating a more refined lens model for both galaxies.

The lensing mass of SNL-0 is robustly determined from earlier *HST* observations (Smith & Lucey 2013). SNL-0's nearly complete Einstein ring lensing configuration provides accurate constraints on the mass model, with a 4 per cent uncertainty. By contrast, SNL-1 and SNL-2 are two-image systems for which previous lensing analysis combined weak lensed-image positional constraints from SINFONI with low-resolution 2MASS imaging (SLC15). The estimated mass uncertainties were 5 and 10 per cent, respectively, due to the unknown contribution from external effects (i.e. shear).

In this paper, we present improved mass estimates for SNL-1 and SNL-2, by exploiting recently acquired *HST* imaging. In Section 2, we outline the data and our reduction procedures. In Section 3, we will provide a visual inspection of these galaxies, along with photometric analysis. In Section 4, we analyse the lensing geometry with multiple parametric models, building upon the previous work and exploiting newly measured lensed image flux ratios. Finally, in Section 5, we summarize these results and compare them to SLC15.

We use parameters from the 7-yr *Wilkinson Microwave Anisotropy Probe* (*WMAP*) when required, i.e. $H_0 = 70.4$ km s^{-1} Mpc^{-1}, $\Omega_m = 0.272$ and $\Omega_\Lambda = 0.728$ (Komatsu et al. 2011). All quoted magnitudes are in the vega system.

2 DATA

We observed SNL-1 and SNL-2 using *HST* Wide Field Camera 3 (WFC3), Uv-VISual (UVIS) channel, in GO cycle 23, (PI: R. Smith). We acquired three dithered *F814W* exposures for each target, for a total of 1050/1002 s, respectively. We took a further three dithered exposures totalling 4413/4272 s, selecting a filter short of the 4000 Å break for the lens-galaxy, but longer than any potential line-of-sight Ly α absorption in the source galaxy spectrum. Due to the differing redshifts of the lens-galaxies, SNL-1 was observed using *F336W*, and SNL-2 in *F390W*.

We post-processed CALWF3 pipeline reduced UVIS data using the ASTRODRIZZLE software (Gonzaga 2012). The images were drizzled on to a cosmic ray rejected final frame with a pixel scale of 0.025, arcsec pixels^{-1}. Due to the limited number of frames in each passband, some artefacts remain after this process, which were masked in the subsequent analysis.

3 LENS AND SOURCE PROPERTIES

In this section, we report our measurements from the *HST* imaging. This includes: (i) morphological descriptions of the lens and the lensed sources, (ii) improved measurements of the lensed-image positions and their relative fluxes, and (iii) independent measurements of the lens structural properties. The relevant parameters are summarized in Table 1.

SNL-1

Extracted regions from the *HST* imaging for SNL-1 are shown in Fig. 1(a–d). SNL-1 displays a regular E/S0 morphology, with an ellipticity of ∼0.4 (measured at the half-image separation from an ELLIPSE fit), and slightly discy isophotes. SNL-1 was shown to be a fast rotator by Newman et al. (2017), and the HST imaging reveals dust obscuration within the central region (∼1 arcsec, Fig. 1b). This suggests the presence of a small cold interstellar medium disc.

The *HST* imaging confirms the two-image system discovered from previous SINFONI data. In Fig. 1(d), we see internal structure in the background source. The outer image, A, displays a clumpy structure with a bright core, implying a late type galaxy. Little structure is visible in the inner image. From the new imaging, we improve the locational constraints of the lensed images, and measure a half-image separation of 2.43 ± 0.03 arcsec, which is 2 per cent larger than in SLC15. We derive the uncertainty from our ability to define centroids for the lensed images internal structure. The observed flux ratio (A/B) is 2.2 ± 0.1, measured from aperture photometry within a lens galaxy subtracted image.

We measure the total lens flux with a two part model. The first component is a direct summation of the flux inside an elliptical aperture with a radius set at a preliminary estimate for R_{eff}. The second component derives the flux contribution outside this region with a 1D Sérsic fit to the outer profile. We find the total magnitude to be $I_{F814W} = 12.75 \pm 0.05$, and a half-light radius of 3.90 ± 0.03 arcsec. This is ∼20 per cent larger than the low S/N 2MASS-based R_{eff} measurement reported in SLC15.

For consistency with previous work, we adopt a fiducial aperture of $R_{ap} = 2.38$ arcsec (the half-image separation derived by SLC15) when quoting magnitude measurements. We find $I_{F814W}(\leq R_{ap}) = 13.85 \pm 0.02$. Combined with the J band measured in SLC15, we measure an $(I_{F814W} - J)$ colour of 1.05, which is consistent with the range of 1.01–1.07 derived for old metal-rich populations from synthesis models (Conroy, Gunn & White 2009).
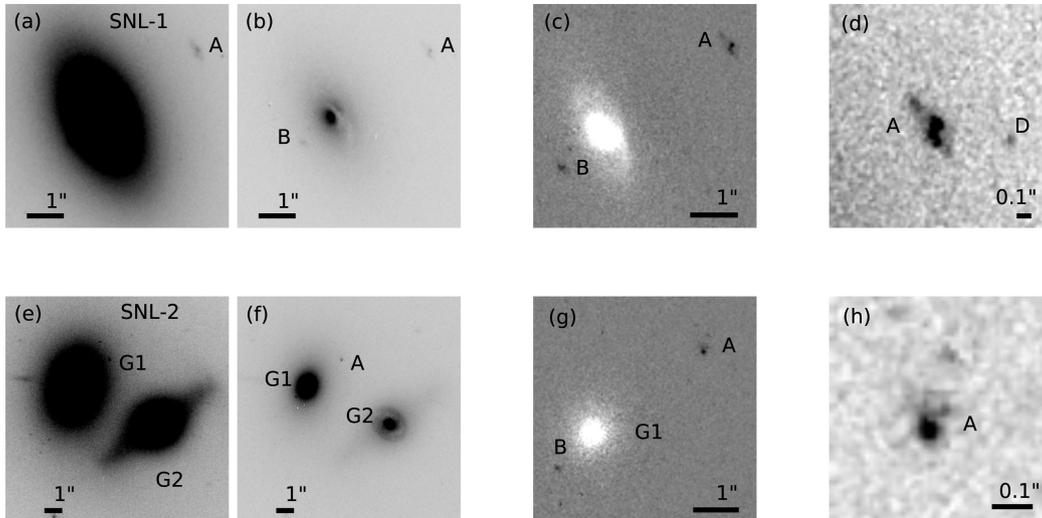
Figure 1. Panels (a-d) show SNL-1. A is the outer, and B the inner lensed image. (a) *F814W* image showing the lens ellipticity. (b) *F336W* image showing the inner obscuration from a disc. (c) scaled *F336W* with *F814W* subtracted for improved contrast of the lensed images. (d) detail of the outer image, A; there is a faint object D, which may or may not be associated. Panels (e-h) show SNL-2, G1 is SNL-2, G2 is the companion galaxy, with A the outer, and B the inner lensed image. (e) *F814W* image containing the lens and companion (f) *F390W* image showing the star formation ring in G2. (g) Scaled *F390W* with *F814W* subtracted for improved contrast of the lensed images. (h) the outer image, showing a compact core with a potentially associated diffuse structure.

SNL-2

We present the *HST* imaging of SNL-2, in Fig. 1(e-h). SNL-2 is confirmed to have an elliptical morphology, with a smooth light profile, and no discernible additional structure. However, SNL-2 lies with a nearby galaxy within a common, extensive and non-symmetric diffuse light halo. The companion, G2, located ∼7 arcsec away, is an edge on late-type galaxy, with disc and bulge components. A star forming ring within the companion's central bulge is seen in Fig. 1(f).

SNL-2 is confirmed to have a two-image lensing system, as found in the original SINFONI discovery data. The bright outer image, A, is a compact object, shown in Fig. 1(h). We clearly observe a bright central region, with a tentatively associated low-brightness structure extending outwards in a single direction. It is possible that an active galactic nucleus (AGN) dominates the flux of SNL-2's source. From the imaging, we measure a half image-separation of 2.30 ± 0.03 arcsec (a 4 per cent increase on SLC15), with an uncertainty from our ability to centroid the unresolved source, and a flux ratio (A/B) of 2.5 ± 0.1.

Due to the more complex local environment of SNL-2, we use GALFIT (Peng et al. 2002) to model and subtract the companion. We model the companion with a Sérsic bulge, and a $n \approx 1$ Sérsic disc. Then we fit SNL-2's light profile following the procedure used for SNL-1. We measure a total magnitude of $I_{F814W} = 13.80 \pm 0.10$, and an effective radius of 3.25 ± 0.03 arcsec. This is significantly smaller than the 6 arcsec measured by SLC15, from low S/N 2MASS imaging. However, the complexity of SNL-2 with a bumpy, asymmetric light halo and companion galaxy limits the accuracy achievable when modelling this two-galaxy system.

As with SNL-1, we measure the magnitudes within a fiducial radius, in this case adopted as $R_{ap} = 2.21$ arcsec, shown in Table 1. The $(I_{F814W}$–$J)$ colour of 1.00 is slightly bluer than the synthesis model predictions of 1.04–1.11 for old metal-rich populations (Conroy et al. 2009).

4 LENS MODELLING

The main aim for this study, is to improve the mass estimates for SNL-1 and SNL-2 beyond the basic treatment in SLC15. We use the LENSMODEL code (Keeton 2001) to create parametrized profiles for each lensing system, informed by the *HST* imaging under the assumption that stellar mass dominates the lensing deflections. We measure the profiles' normalization, from which we extract the mass enclosed within the fiducial radius (R_{ap}, from Table 1). In Section 4.1, we apply only the improved image position constraints. Then in Section 4.2, we include information from image-flux measurements to break the degeneracy between mass and external shear for SNL-1, and constrain the companion's effect in SNL-2. The results of our analysis are summarized in Table 2.

4.1 Positional constraints

For SNL-1, we start our analysis with a singular isothermal sphere (SIS). This is the closest model to the spherical symmetry used in SLC15. From the SIS model, we measure $M(\leq R_{ap}) = 9.48 \times 10^{10} M_{\odot}$, 2 per cent larger than the previous estimate, due to the increased image separation. Fig. 1(a) shows SNL-1 to have significant ellipticity, and to be orientated off-axis to the image separation. We incorporate this using a singular isothermal ellipsoid (SIE) profile with a fixed ellipticity of 0.4. The resulting enclosed mass is ∼7 per cent smaller than predicted using a SIS model.

As the stellar mass dominates within R_{Ein}, we create a pixelized mass-follows-light (MFL) profile for the mass distribution. For the light profile, we use an IRAF ELLIPSE fit (Jedrzejewski 1987), to minimize contamination from both the dust lane and the lensed images, as the basis for the mass profile. We assume the surface mass density is proportional to the surface brightness, such that the resulting model normalization is the mass-to-light ratio. The MFL estimated mass is ∼3 per cent smaller than the SIS model.

For SNL-2, we begin with a simplified case, in which we neglect the companion, and follow the procedure for SNL-1. The SIS

Table 2. Lens mass estimates from LENSMODEL in units of $10^{10}\,M_\odot$. Masses are measured within the fiducial radius, R_{ap}. However the values are derived from the *HST* data and refined mass models. The mass estimates adopted for the conclusions are denoted in bold.

Model	SNL-1	SNL-2	Notes
Constrained by image positions, no shear			
SLC15	9.27	13.07	Table 2, No f_{corr}
SIS	9.48	13.62	
SIE	8.78	14.11	
MFL	9.22	13.42	
Constrained by flux ratio and positions, with shear (Shear)			
SIS + γ	9.08	–	+4.3 per cent
SIE + γ	9.57	–	−8.8 per cent
MFL + γ	9.41	–	−2.1 per cent
Constrained by image positions with companion (Flux ratio)			
MFL + SIS	–	12.83	3.28
MFL + SIE	–	12.87	3.26
MFL + MFL	–	13.15	3.75
Constrained by flux ratio, positions with companion			
MFL + SIS	–	12.28	
MFL + SIE	–	12.38	
MFL + MFL	–	12.69	
Adopted Mass	**9.49 ± 0.15**	**12.59 ± 0.30**	

model mass is ∼4 per cent larger than in SLC15, attributable to the larger *HST* measured image separation. We observe that SNL-2, like SNL-1, has a non-zero ellipticity and so model an SIE case, which increases the estimated mass by ∼4 per cent. We form a MFL profile for SNL-2, from an ELLIPSE fit to a companion-subtracted *F*814*W* image, which will account for structure in the light profile. The MFL model estimates $M(\leq R_{ap})$ to be ∼1.5 per cent smaller than SIS model.

4.2 Flux constraints

The previous lensing solutions assume an isolated lens galaxy. In reality, the local environment causes a measurable effect on the lensing configuration, resulting in a degeneracy between mass and external shear (γ). An external shear causes an expansion along a given axis, and a perpendicular compression. We define a positive/negative shear to represent expansion/compression dominating in the image-separation axis, which reduces/increases the required enclosed mass for a given set of image positions. As the shear factor varies, the magnification of each image from a lensed source will change (illustrated for SNL-1 in Fig. 2). The observed flux ratio, acting as a proxy for relative magnification of the lensed images, can therefore break this degeneracy between mass and shear.

For SNL-1, we constrain the shear using the measured flux ratio (A/B) of 2.2 ± 0.1, and show the resultant masses in Table 2. For the SIE and MFL profiles this method recovers a compressive (negative) shear, increasing the measured lensing mass by ∼9 and ∼2 per cent, respectively. (The SIS is less well defined, as the shear factor accounts for the combined effects of ellipticity, orientation and shear in this case.) Adopting the SIE+γ and MFL+γ models, we derive limits on $M(\leq R_{ap})$ from model-to-model uncertainty, within the flux ratio bounds, to be $9.34 - 9.64 \times 10^{10}\,M_\odot$, which is shaded in Fig. 3.

For SNL-2, the close companion galaxy likely dominates the external mass distribution. We constrain the companion galaxy's
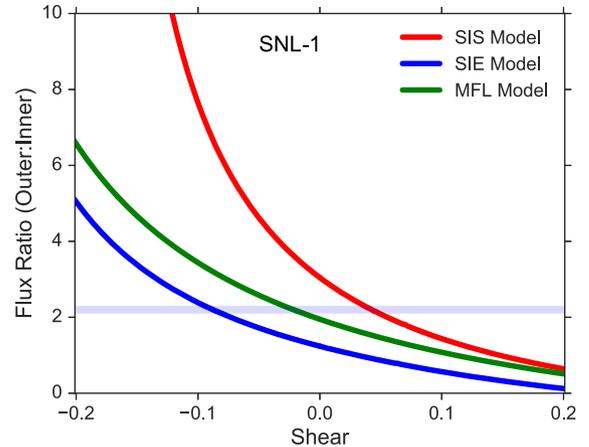

Figure 2. The external shear for given fixed image positions will modify the magnification each lensed image is subject to. We show this for SNL-1, comparing the predicted flux ratio of the lensed images to the shear. We shade in blue the measured flux ratio range of 2.2 ± 0.1, indicating a weak compressive (negative) shear along the image-separation axis, for the SIE and MFL models.
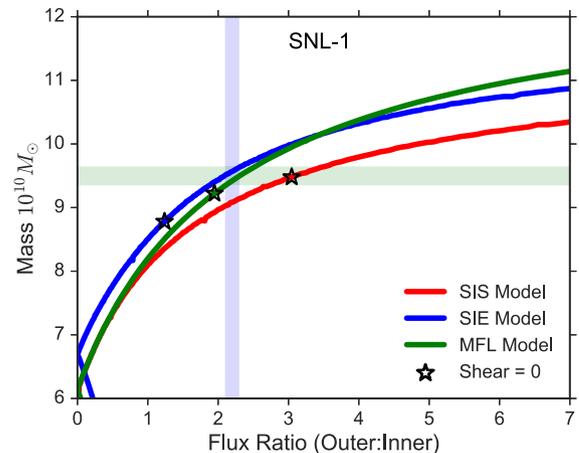

Figure 3. The model predicted flux ratio against mass for the three primary lens models of SNL-1. We shade the measured flux ratio of 2.20 ± 0.1 in blue, from which we estimate the mass range breaking the mass versus shear degeneracy. The star symbols display the mass estimated for the case of no external shear. The mass range estimated by the SIE and MFL models for SNL-1 is shaded in green.

contribution with the measured flux ratio, similar to the method for SNL-1. We treat SNL-2 with a MFL model throughout, and consider SIS, SIE and MFL descriptions for the secondary. We use these two-component models to predict the flux ratio as a function of the companion's mass normalization. In Fig. 4, we compare the total lensing mass to the observed flux ratio (A/B), of 2.5 ± 0.1. We find close agreement between the SIS and SIE secondary models, with significant divergence in the MFL case towards low flux ratios. As the companion is external to the primary lens configuration, we must consider its extended profile, and thus total (stars plus DM) mass. We therefore prefer the isothermal models for our treatment of the companion.

As shown in Fig. 4, there are no models that match both the image positions and the observed image flux ratio. The models that reproduce the measured flux ratios yield a lensing mass of $\sim 12.33 \times 10^{10}\,M_\odot$, but lead to an offset of ∼0.1 arcsec between the observed and predicted image positions. The models that best
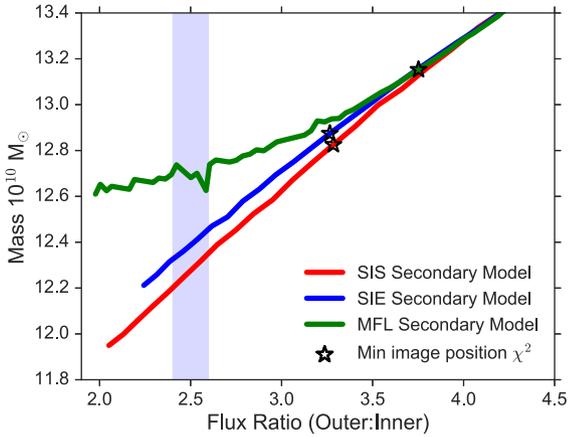
Figure 4. The modelled mass for SNL-2 against flux ratios for a varying mass companion. The shaded region defines the measured flux ratio of 2.5 ± 0.1, with the black symbols indicating the best fit for the image positions. In order to fit the measured flux ratio, the offset in image position is ~ 0.1 arcsec.

fit the image positions lead to a comparatively heavier primary lens, with a mass of $\sim 12.85 \times 10^{10} \, M_\odot$.

The deviation between measured and predicted flux ratios in our modelling, (2.5 and ~ 3.3, respectively) seen in Fig. 4, corresponds to ~ 0.3 magnitudes. The compact nature of the source galaxy tentatively suggests a flux dominated by AGN activity, and for such a source microlensing can cause a discrepancy between the measured and predicted flux ratios of the order of a few tenths of a magnitude (e.g. Schechter & Wambsganss 2002; Schechter et al. 2014). Alternatively, a similar effect may result from intrinsic AGN variability combined with lensing path-length differences. These factors preclude obtaining an improved lensing mass estimate for this galaxy with the present data.

5 DISCUSSION AND CONCLUSION

The newly acquired *HST* data has revealed insights into the two-image lensing systems from SNELLS, including uncovering evidence for a previously unknown dust disc within the fast rotating SNL-1. We improved upon previous strong lensing analysis using the *HST* data to break the mass-versus-shear and companion degeneracies for SNL-1 and SNL-2, respectively. We measure precise lensed-image positions, and reliably quantify the lensed-image flux ratio, which was not possible with the SINFONI discovery data. We compare our adopted masses, shown in Table 2, to those of SLC15, and estimate the stellar mass-to-light ratio (Υ). Furthermore, combining the measured mass and luminosity in this paper, with the spectroscopically fit Kroupa reference stellar mass-to-light ratio ($\Upsilon_{\rm ref}$) (Newman et al. 2017, table 1) (converted to I_{F814W} from the r-band, with EZGAL), we independently estimate the IMF mismatch parameter α within the fiducial radius ($R_{\rm ap}$).

For SNL-1, we adopt a final lensing mass estimate of $M(\leq R_{\rm ap}) = 9.49 \pm 0.15 \times 10^{10} \, M_\odot$, from the SIE+$\gamma$ and MFL+γ models. The quoted error is derived from the spread between lens profiles incorporating the flux ratio uncertainty. Due to the extended nature of the source, the contribution from microlensing is negligible. The positional errors provide a formal uncertainty of ≤ 0.5 per cent. We obtain the stellar mass by subtracting the EAGLE DM mass contribution estimated in SLC15 (~ 15 per cent) from the lensing mass. The estimated I_{F814W} measured $\Upsilon_{\rm R_{ap}}$ is 3.21 ± 0.12, and so combined with the converted $\Upsilon_{\rm ref}$ of 2.75 (Newman et al. 2017), we derive

$\alpha = 1.17 \pm 0.09$. This is 3 per cent smaller than 1.20 ± 0.13 found by SLC15.

For SNL-2, the final lensing mass estimate is $M(\leq R_{\rm ap}) = 12.59 \pm 0.30 \times 10^{10} \, M_\odot$, derived from the MFL+SIS, and MFL+SIE models for the two regimes in Table 2. The uncertainty is dominated by tension between the measured and predicted flux ratios. Following the SLC15 EAGLE DM procedure, and incorporating the newly measured I_{F814W} luminosity, we estimate $\Upsilon_{\rm R_{ap}}$ to be 2.49 ± 0.15. With the converted $\Upsilon_{\rm ref} = 2.59$, we obtain $\alpha \simeq 0.96 \pm 0.10$. This is a 2 per cent increase upon 0.94 ± 0.17 measured by SLC15.

In conclusion, our analysis of higher resolution and deeper imaging of SNL-1 and SNL-2 from *HST* supports the lensing masses, and the IMF α factors, estimated by SLC15. For SNL-2, further caution is required due to the complexity in modelling its source and companion galaxy. For SNL-1 the results show that the discrepancies in α reported by Newman et al. (2017) cannot be attributed to the simplistic assumptions of the SLC15 lens modelling. Future stellar- and gas-dynamical studies of SNL-1 should help to resolve this specific puzzle, and perhaps by implication begin to provide an explanation for the broader issue of agreement between the various methods for constraining the IMF.

REFERENCES

Campbell L. A. et al., 2014, MNRAS, 443, 1231
Cappellari M. et al., 2012, Nature, 484, 485
Conroy C., van Dokkum P. G., 2012, ApJ, 760, 71
Conroy C., Gunn J. E., White M., 2009, ApJ, 699, 486
Courteau S. et al., 2014, Rev. Mod. Phys., 86, 47
Gonzaga S., 2012, The DrizzlePac Handbook. Space Telesc. Sci. Inst., Baltimore
Jedrzejewski R. I., 1987, in de Zeeuw P. T., ed., Proc. IAU Symp. 127, Structure and Dynamics of Elliptical Galaxies. Kluwer, Dordrecht, p. 37
Keeton C. R., 2001, ApJ, preprint (arXiv:astro-ph/0102340)
Komatsu E. et al., 2011, ApJS, 192, 18
Kroupa P., 2001, MNRAS, 322, 231
Mancone C. L., Gonzalez A. H., 2012, PASP, 124, 606
Navarro J. F., Frenk C. S., White S. D. M., 1996, ApJ, 462, 563
Newman A. B., Smith R. J., Conroy C., Villaume A., van Dokkum P., 2017, ApJ, 845, 157
Peng C. Y., Ho L. C., Impey C. D., Rix H.-W., 2002, AJ, 124, 266
Schechter P. L., Wambsganss J., 2002, ApJ, 580, 685
Schechter P. L., Pooley D., Blackburne J. A., Wambsganss J., 2014, ApJ, 793, 96
Schlafly E. F., Finkbeiner D. P., 2011, ApJ, 737, 103
Smith R. J., Lucey J. R., 2013, MNRAS, 434, 1964
Smith R. J., Blakeslee J. P., Lucey J. R., Tonry J., 2005, ApJ, 625, L103
Smith R. J., Lucey J. R., Conroy C., 2015, MNRAS, 449, 3441
Treu T., 2010, ARA&A, 48, 87
Treu T., Auger M. W., Koopmans L. V. E., Gavazzi R., Marshall P. J., Bolton A. S., 2010, ApJ, 709, 1195

This paper has been typeset from a TeX/LaTeX file prepared by the author.